Towards Understanding the Variation of Electrode Design Parameters on the Electrochemical Performance of Aluminum Graphite Batteries

An Experimental and Simulation Study

Appiah, Williams Agyei; Stockham, Mark P.; Lastra, Juan Maria Garcia

Published in:
Batteries and Supercaps

Link to article, DOI:
10.1002/batt.202300258

Publication date:
2023

Document Version
Publisher's PDF, also known as Version of record

Batteries & Supercaps

Research Article
doi.org/10.1002/batt.202300258

Chemistry Europe
European Chemical Societies Publishing

www.batteries-supercaps.org

Towards Understanding the Variation of Electrode Design Parameters on the Electrochemical Performance of Aluminum Graphite Batteries: An Experimental and Simulation Study

Williams Agyei Appiah,*[a] Mark P. Stockham,[b] and Juan Maria Garcia Lastra*[a]

Due to their high power density and availability, aluminum batteries consisting of graphite positive electrode and ionic liquid electrolytes are promising candidates for post-lithium-ion batteries. However, the effect of the various electrode design parameters on their electrochemical performance is not well understood. Herein, a high-fidelity physics-based model validated with experimental data obtained from a Swagelok cell consisting of an aluminum metal negative electrode, imidazolium ionic liquid electrolyte, and graphite positive electrode is used to study the effects of various electrode design parameters on the discharge capacity. The model is used to optimize the design of the electrodes by generating several Ragone plots, estimating the optimum current density for a given cell design, and explaining the limitations of the cells based on the transport of the electroactive species. An optimum graphite thickness of 50 μm is obtained for all the discharge times considered in this study. Determining the ideal electrode configuration for Al-graphite batteries using different ionic liquid electrolytes and considering various discharge durations could provide a reference point for evaluating the suitability of a specific ionic liquid electrolyte in a particular use case.

Introduction

Rechargeable aluminum batteries (RABs) that utilize ionic liquid (IL) electrolytes have emerged as promising energy storage devices. They are favored due to the ease of processing the IL electrolyte, the abundance of aluminum, and the combination of high power density and stability achieved when using graphite as the positive electrode.[1–6] Nonetheless, several factors, including the cost of the IL electrolyte, specific energy, average specific power, reliability, and safety, must be considered simultaneously during the battery design process for a particular application. The cost and lifespan of aluminum batteries primarily hinge on the selection of active positive electrode materials[7–9] and electrolyte choice.[10–12] At the same time, the specific energy and average specific power are heavily influenced by the cell design.[13,14] Therefore, considerable effort is required regarding cell design and material selection when seeking a suitable RAB for a specific application.

[a] Dr. W. A. Appiah, Prof. J. M. Garcia Lastra
Department of Energy Conversion and Storage
Technical University of Denmark
Kgs. Lyngby, 2800 (Denmark)
E-mail: wagap@dtu.dk
jmgla@dtu.dk

[b] Dr. M. P. Stockham
School of Chemistry
University of Southampton
Southampton SO17 1BJ (United Kingdom)

Designing a cell for a specific application involves time-consuming and expensive experiments to optimize the electrode's thickness and porosity. An efficient alternative is using physics-based models and simulations[15,16] that have been experimentally validated. These models can provide guidelines for cell design and enhance understanding of the limitations associated with a particular design. Previous studies have focused on optimizing electrode design for lithium-ion batteries (LIBs) by employing physics-based models,[13,14,17,18] machine-learning approaches,[19,20] and experimental techniques.[21,22] For example, Srinivan et al.[14] and Appiah et al.[13] utilized comprehensive physics-based models to optimize the porosity and thickness of the $LiFePO_4$ and $LiNi_{0.6}Co_{0.2}Mn_{0.2}O_2$ positive electrodes, respectively, while keeping other cell design parameters constant for various LIB applications based on discharge time. These studies determined the optimal cell design by maximizing the specific energy achieved, as thicker and denser electrodes result in higher capacity due to increased Li ions with increased positive electrode thickness. However, in the case of rechargeable aluminum batteries (RABs) with graphite positive electrodes, the electroactive species primarily originates from the IL electrolyte.[15] Consequently, variations in positive electrode thickness would not significantly impact the specific energy. Therefore, a new parameterization and methodology are necessary for designing electrodes specifically for RABs.

Herein, we propose an optimization method for RABs based on estimating current density and generating Ragone plots using a high-fidelity physics-based model developed for Al-graphite batteries with EMIMCl-$AlCl_3$ IL electrolytes. The fidelity of the developed model is verified by comparing the model's predicted discharge voltage profiles with experimental data

Research Article
doi.org/10.1002/batt.202300258
Chemistry Europe
European Chemical Societies Publishing

obtained from a Swagelok cell consisting of an Al negative electrode, graphite positive electrode, and EMIMCl-$AlCl_3$ IL electrolytes. We used the model together with a non-linear least square technique, namely, the Nelder Mead algorithm, to study the effects of the different positive electrode thicknesses and porosities on the transport of the electroactive species, $AlCl_4^-$, in the solution and solid phase of the graphite positive electrode. This was achieved by fitting the model-predicted discharge profiles to those of the experiments. To determine the optimal current density for a given application, we adopted the optimization method originally proposed by Tiedemann and Newman[23] to optimize the thickness and porosity of the graphite positive electrode while holding the concentration of the electroactive species and other cell design parameters constant.

Model Development

The schematic diagram of the cell modeled in this work and the reaction path considered the Al-IL interphase are presented in Figure 1. The cell consists of a Molybdenum current collector, a natural graphite positive electrode, and two Whatman GF/F glass microfiber separators assembled in a Swagelok cell. The pores in the positive electrode and separator are filled with an EMIMCl-$AlCl_3$ (molar ratio of 1:1.5) IL electrolyte. The model considers the transport of the $AlCl_4^-$ species from the graphite positive electrode through the separator to the Al negative electrode, where it undergoes a dissociation-oxidation-chlorination reaction to produce $Al_2Cl_7^-$ species. The $Al_2Cl_7^-$ species are transported into the bulk electrolyte. Density Functional Theory (DFT) simulations in previous work[24] determined the dissociation-oxidation-chlorination reaction path. This work showed that the chlorination reaction does not significantly influence the stripping/discharge mechanism; hence we did not include the dissociation and chlorination effect in this work. Thus five main rate-determining steps were considered in this model; (i) charge transfer at the graphite/IL electrolyte interface, (ii) diffusion of $AlCl_4^-$ species within the graphite positive electrode, (iii) decumulation of $AlCl_4^-$ concentration from the saturation level, y in $C_n[AlCl_4]_{(1-y)}$, (iv) transport of $AlCl_4^-$ species through the pores of the graphite positive electrode and separator, and (v) charge transfer at the Al/IL electrolyte interface.

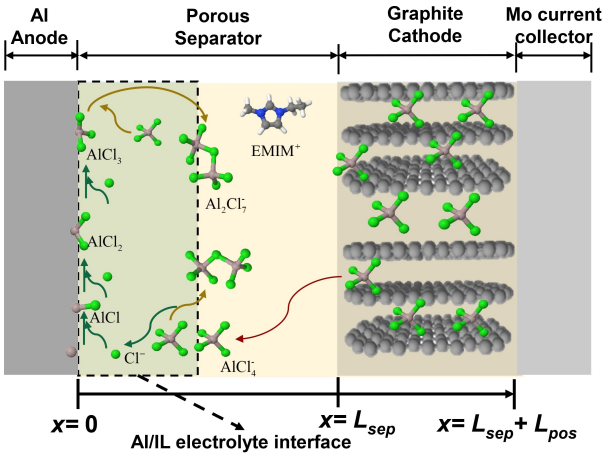

Figure 1. Schematic diagram of the aluminum chloride graphite cell with EMIMCl-$AlCl_3$ IL electrolyte cell modeled in this work with various chlorination reactions at the Al-IL interface during discharge.

The reaction mechanisms at the Al/IL electrolyte interface can be described based on chronoamperometry[25] and ^{27}NMR[26] experiments as

$$Al + 7AlCl_4^- \xrightarrow{\text{discharge}} 4\ Al_2Cl_7^- + 3e^- \quad (1)$$

At the graphite positive electrode/IL electrolyte interface, graphite undergoes a reduction process according to the reaction,[2,27]

$$C_n\left[AlCl_4^-\right]_{(1-y)} + ye^- \xrightarrow{\text{discharge}} C_n + yAlCl_4^- \quad (2)$$

where y is the mole fraction of intercalated $AlCl_4^-$ species into the graphite.

Governing equations–porous separator

The material balance for species k is described as.

$$\varepsilon_{sep}\frac{\partial c_k}{\partial t} = -\nabla \cdot N_k \quad (3)$$

where ε_{sep} and c_k are the porosity of the separator and the concentration of species k ($k = Al_2Cl_7^-$, $AlCl_4^-$, $EMIM^+$), respectively. The flux N_k is based on the Nernst-Plankt equation and is given as

$$N_k = -\varepsilon_{sep}D_k\nabla c_k - z_k\frac{\varepsilon_{sep}D_k}{RT}Fc_k\nabla\Phi_2 \quad (4)$$

where D_k and z_k are the diffusion coefficient and the charge number of species k, respectively.Φ_2 is the liquid phase potential. The diffusion coefficients of the species in the liquid-phase is estimated using Stokes-Einstein relation : $D_k = \frac{RT}{6\pi N_A \eta r}$, R is the gas constant (8.3145 J mol K), T is the absolute temperature, N_A is Avogadro's number, η is the viscosity (13 mbar)[28] and r is the radius of the species. The values obtained are similar to that obtained experimentally.[29] Table 1 shows the transport parameters and reference concentrations.

Governing equations–porous positive electrode

The material balance on the individual species, k, ($k = Al_2Cl_7^-$, $AlCl_4^-$, $EMIM^+$) in the IL electrolyte that occupies the porous part of the positive electrode is given by

$$\varepsilon_1\frac{\partial c_k}{\partial t} = -\nabla \cdot N_k + R_2 \quad (5)$$

Research Article
doi.org/10.1002/batt.202300258
Chemistry Europe
European Chemical Societies Publishing

Table 1. Transport parameters and reference concentrations.

Species (k)	z_k	Radius [nm]	D_k^0[m^2s^{-1}]	$C_{k,ref}$[mol m^{-3}]
$Al_2Cl_7^-$	−1	0.46[a]	3.65×10^{-11}	1960 [b]
$AlCl_4^-$	−1	0.31[a]	5.42×10^{-11}	1960 [b]
EMI+	+1	0.18[a]	4.31×10^{-11}	3920 [b]

[a] Parameters obtained from the literature [Ref. <29>].[b] Parameters based on experimental design.

where R_2 is the production rate of $AlCl_4^-$ species at the positive electrode/IL electrolyte interface and $\varepsilon_1$is the porosity of the positive electrode. R_2 is expressed as a function of the current density, $i_{1,p}$, and the potential drop across the positive electrode/IL electrolyte interface, η_p as

$$R_k = -\frac{a_v s_k}{nF} i_{1,p} \tag{6}$$

where a_v is the specific surface area of the positive electrode, n is the number of electrons, $s_{k,}$ is the stoichiometric coefficient of the species in electrochemical reaction 2, occurring at the positive electrode/IL electrolyte interface. The Butler-Volmer equation is used to describe the current density, $i_{1,p}$, which is given as

$$i_{1,p} = i_{0,p}\left[(1-\theta)\left(\frac{c_{AlCl_4^-}}{c_{AlCl_4^-,ref}}\right)\boldsymbol{exp}\left(\frac{0.5F}{RT}\eta_p\right) - \theta\boldsymbol{exp}\left(-\frac{0.5F}{RT}\eta_p\right)\right] \tag{7}$$

where $i_{0,p}$ is the exchange current density, θ is the relative saturation of $AlCl_4^-$ species in the solid phase ($\theta = \frac{c_{AlCl_4^-,s}}{c_{AlCl_4^-,smax}}$), and the overpotential, η_p, is expressed as

$$\eta_p = \Phi_1 - \Phi_2 - U_p^0 \tag{8}$$

where Φ_1, Φ_2 and U_p^0 are the solid phase, liquid phase, and open circuit potential, respectively. The open circuit potential of the graphite positive electrode U_p^0 is expressed as a function of the mole fraction of intercalated $AlCl_4^-$ species into the graphite, y, as

$$U_p^0 = 0.72 + 0.14y + 0.03x^{0.5} - \frac{0.02}{y} + \frac{0.001}{y^{1.55}} + 0.51exp(0.90 - 18.7y) \; - 0.83exp(0.42y - 0.41) \tag{9}$$

Based on electroneutrality, the positive and negative charges must be using the following expression,

$$\nabla \cdot i_1 + \nabla \cdot i_2 = 0 \tag{10}$$

where i_1 and i_2 denote the current density in the solid and liquid phases, respectively. Ohm's law governs the charge transfer in the solid phase

$$i_{1,p} = -\sigma \; \nabla \; \Phi_1 \tag{11}$$

where σ is the conductivity of the graphite positive electrode. The current density in the solution phase is given by

$$i_2 = F\sum_k z_k N_k \tag{12}$$

A charge constraint equations was applied to ensure that the transport of charges at positive electrode/IL electrolyte interface and the Al/IL electrolyte interface was controlled by the electrochemical reactions and is expressed as

$$\nabla \; i_2 = a\sum\left(i_{1,i}\right) \; i = p, n \tag{13}$$

The rate of the electrochemical reactions occurring at the Al/IL electrolyte interface, $i_{1,n}$ is described by the Buttler-Volmer equation as,[30]

$$i_{1,n} = nq\left[\left(K_1^a\right)\boldsymbol{exp}\left(\frac{0.5F}{RT}\eta_n\right) - \left(K_1^c\right)\boldsymbol{exp}\left(-\frac{0.5F}{RT}\eta_n\right)\right] \tag{14}$$

where q is the charge number, K_1^a and K_1^c are the anodic and cathodic rate constants expressed based on transition-state theory as

$$K_1^a = \left(\frac{k_B T}{h}\right)Ae^{-\left(\frac{E_a}{RT}\right)}\prod_{(k)}\left[\frac{c_k}{c_{ref,k}}\right]^{p_{(k)}} \tag{15}$$

$$K_1^c = \left(\frac{k_B T}{h}\right)Ae^{-\left(\frac{E_a}{RT}\right)}\prod_{(k)}\left[\frac{c_k}{c_{ref,k}}\right]^{q_{(k)}} \tag{16}$$

where k_B is the Boltzmann constant, h is the Planck constant, T is the operating temperature, A is the area factor, and E_a is the energy barrier for the individual electrochemical reaction (1). The energy barrier for the forward and backward reactions is assumed to be the same. $p_{(k)}$ and $q_{(k)}$ are the coefficients for the products and reactants involved in the electrochemical reactions 1. The overpotential η_n for reaction (1) is expressed as

$$\eta_n = \Phi_1 - \Phi_2 - U_n^0 \tag{17}$$

The equilibrium potential for the striping and plating of Al according to the electrochemical reaction 1 is determined by Nernst's equation and is expressed as

$$U_n^0 = \frac{RT}{3F} ln \frac{\left[c_{\left(Al_2Cl_7^-\right)}\right]^4}{\left[c_{\left(AlCl_4^-\right)}\right]^7} \quad (18)$$

The transport of $AlCl_4^-$ species in the solid phase of the graphite positive electrode is assumed to be governed by Fick's second law and is expressed as

$$\frac{\partial c_{AlCl_4^-}}{\partial t} = D_{AlCl_4^-}\left(\frac{\partial^2 c_{AlCl_4^-}}{\partial x^2}\right) \quad (19)$$

where $D_{AlCl_4^-}$ is $AlCl_4^-$ species within the graphite positive electrode. From our parameter estimation analysis involving fitting the model prediction to the experimental data, we observed a two-phase reaction in the graphite particles at high current densities and thicker electrodes. To account for this, we expressed the diffusion coefficient as a function of the state of charge (SOC) as follows,

$$D_{AlCl_4^-} = \frac{D^0_{AlCl_4^-}}{SOC^2 - 0.4104 \times SOC + 0.0958} \quad (20)$$

where $D^0_{AlCl_4^-}$ is the initial diffusion coefficient.

The discharge capacity at the lower cutoff voltage during a constant current discharging, Q_{dch}, is expressed as

$$Q_{dch} = \int_0^{t=t_{cc}} \varepsilon_s \sigma \frac{\partial \Phi_1}{\partial x}\bigg|_{x=L_{sep}+L_{pos}} dt \quad (21)$$

where ε_s is the volume fraction of the active material in the positive electrode, σ is the conductivity of the positive electrode, Φ_1 is the potential in the solid phase, and L_{sep} and L_{pos} are the thickness of the separator and positive electrode, respectively.

Boundary and initial conditions

We applied five boundary conditions at the positive electrode/current collector interface, ($x = L_{sep} + L_{pos}$), one each for the solid phase, Φ_1 and liquid phase, Φ_2 potential and the remaining three for the concentration of the species in the electrolyte. The flux of each species k ($k = Al_2Cl_7^-$, $AlCl_4^-$, and $EMIM^+$) is set to zero

$$N_k = 0 \quad (22)$$

The current density in the solid phase is set to the applied current density, and the current density in the solution phase at this boundary is equal to zero.

$$-\sigma \nabla \Phi_1 = I_{app} \quad (23)$$

$$i_2 = 0 \quad (24)$$

where I_{app} is the applied constant current.

The boundary condition at the graphite particles/IL electrolyte interface is

$$D_{AlCl_4^-}\left(\frac{\partial c_{AlCl_4^-}}{\partial x}\right) = i_{1,p} \quad (25)$$

At the separator/positive electrode interface ($x = L_{sep}$), the flux of each of the species, k is continuous and can be expressed as

$$N_{k,separator} = N_{k,cathode} \quad (26)$$

The current density in the solid phase at the separator/positive electrode interface is zero according to the equation

$$-\sigma \nabla \Phi_1 = 0 \quad (27)$$

The above boundary conditions indicate the assumption that there is no accumulation of $AlCl_4^-$ species at the positive electrode/electrolyte interface, and there is no transfer of $AlCl_4^-$ species across the positive electrode/current collector interface.

At the beginning of the discharge process (t = 0), the initial concentration of all the species, k is set to the reference concentration, $c_{k,ref}$ values in Table 1. This is mathematically represented as

$$c_k = c_{k,ref} \text{ at } t = 0 \text{ and for all } x \geq 0 \quad (28)$$

The tertiary current distribution module and global Ordinary Differential Equations (ODEs) module in COMSOL Multiphysics were used to solve the developed model equations.

Results and Discussion

Experimental results

The discharge capacities of Al-graphite cells with different positive electrode thicknesses and porosities were analyzed in Figure 2 as a function of the discharge current rate, which ranged from 0.2 C to 5 C. Increasing the current rate for a cell with a specific positive electrode thickness and porosity decreased discharge capacity. However, the impact of the discharge rate on capacity was minimal for the cell with a positive electrode thickness of 30 μm and a porosity of 0.767 (thin and porous electrode), while it was most pronounced for cells with a positive electrode thickness of 86 μm and a porosity of 0.711 (thick and porous electrode). Additionally, the cell with a positive electrode thickness of 22 μm and a porosity of 0.346 (thin and dense electrode) demonstrated a strong dependence of discharge capacity on the current rate. Hence, both positive electrode thickness and porosity significantly influenced the

Research Article
doi.org/10.1002/batt.202300258
Chemistry Europe
European Chemical Societies Publishing

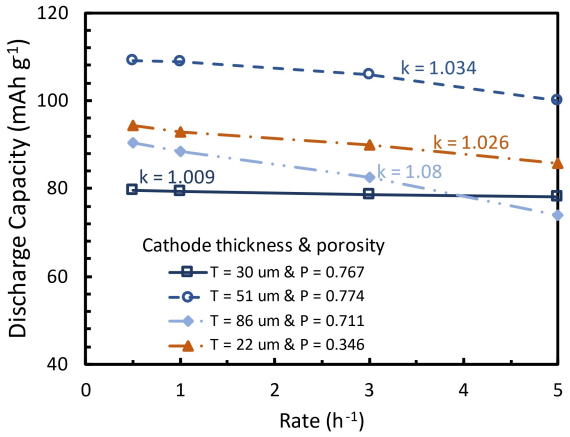

Figure 2. Effects of positive electrode thickness and porosity on the discharge capacity and Peukert coefficients as a function of discharge current rate.

rate performance of Al-graphite cells using EMIMCl-$AlCl_3$ IL electrolyte.

The discharge capacities of Al-graphite cells with different graphite positive electrode thicknesses and porosities were analyzed in Figure 2 as a function of the discharge rate, which ranged from 0.2 C to 5 C. Increasing the current rate for a cell with a specific positive electrode thickness and porosity resulted in a decrease in discharge capacity. However, the impact of the discharge rate on capacity was minimal for the cell with a positive electrode thickness of 30 μm and a porosity of 0.767 (thin and porous electrode), while it was most pronounced for cells with a positive electrode thickness of 86 μm and a porosity of 0.711 (thick and porous electrode). Additionally, the cell with a positive electrode thickness of 22 μm and a porosity of 0.346 (thin and dense electrode) demonstrated a strong dependence of discharge capacity on the current rate. Hence, both positive electrode thickness and porosity significantly influenced the rate performance of Al-graphite cells using EMIMCl-AlCl3 IL electrolyte.

To gain further insights into the rate performance of different electrode designs, we calculated the Peukert coefficients (k) by fitting the discharge capacities of various cells at specified discharge rates to Peukert's law ($C = i^k \times t$, where C represents the theoretical capacity of the cell, t is the nominal discharge time (in hours) for a specific discharge current rate, and i is in A). Peukert's law assumes that all electrode reactions occur completely at a given discharge rate, so a higher Peukert coefficient indicates poorer rate performance. For less dense electrodes, the Peukert coefficient (k) increased with increasing positive electrode thickness (cells with thickness and porosity of 30 μm and 0.767, 51 μm and 0.774, and 86 μm and 0.711, respectively). The cells with dense electrodes exhibited relatively higher values of k (cells with thickness and porosity of 22 μm and 0.346). The cells with a positive electrode thickness of 51 μm and a porosity of 0.774 demonstrated optimal discharge capacities at specific discharge rates. Based on the assumption of Peukert's law, the electrode reactions at the positive electrode/IL electrolyte interface were not completed at the minimum cutoff potential, particularly for cells with thicker and denser electrodes.

Model validation

The accuracy of the model was confirmed by comparing the voltage profiles predicted by the model with experimental data obtained from Al-graphite cells with varying positive electrode thicknesses and porosities at discharge rates of 0.5 C, 1.0 C, 3.0 C, and 5.0 C, and illustrated in Figure 3. The model's predictions, represented by short dashes, were based on the parameters listed in Table 2, while the solid lines depict the experimental data. There was a good agreement between the model predictions and experimental data across all discharge rates. The simulations were conducted under identical conditions for all cases, with the only difference being the positive electrode thickness and porosities.

In the cells with thinner and porous electrodes (Figure 3b), discharge capacities were not significantly changed with increasing discharge current rates. Decreasing the porosity in the thinner electrodes (Figure 3a) increased discharge capacity, while the discharge capacity decreased with higher current rates. Increasing the thickness of porous electrodes (Figure 3c and d) resulted in a higher discharge capacity but with a relatively poorer rate performance. Unlike Li-ion batteries,[13] Al-graphite cells with EMIMCl-$AlCl_3$ IL did not exhibit any changes in the IR drop in the discharge curve with increasing current rates. Nevertheless, there was a loss in discharge capacity at

Table 2. Design adjustable parameters.

Parameter	Description	Value
L_{pos} [a], μm	Thickness of positive electrode	Variable
L_{sep} [a], μm	Thickness of separator	620
$E_{a,strip}$ [b] J mol^{-1}	Activation barrier for stripping	3.92×10^4
R_p [a], μm	Radius of graphite particle	5
$i_{0,p}$ [c], A m^{-2}	Positive electrode exchange current density	1.96
σ [c], S m^{-1}	Conductivity of graphite	100
$c_{AlCl_4^-,smax}$, mol m^{-3}	Maximum solid phase concentration of $AlCl_4^-$	9135

[a] Parameter based on cell design. [b] Nominal parameters based on DFT simulations [Ref. < 24 >]. [c] Parameters obtained from the literature[31]

Research Article
doi.org/10.1002/batt.202300258
Chemistry Europe
European Chemical Societies Publishing

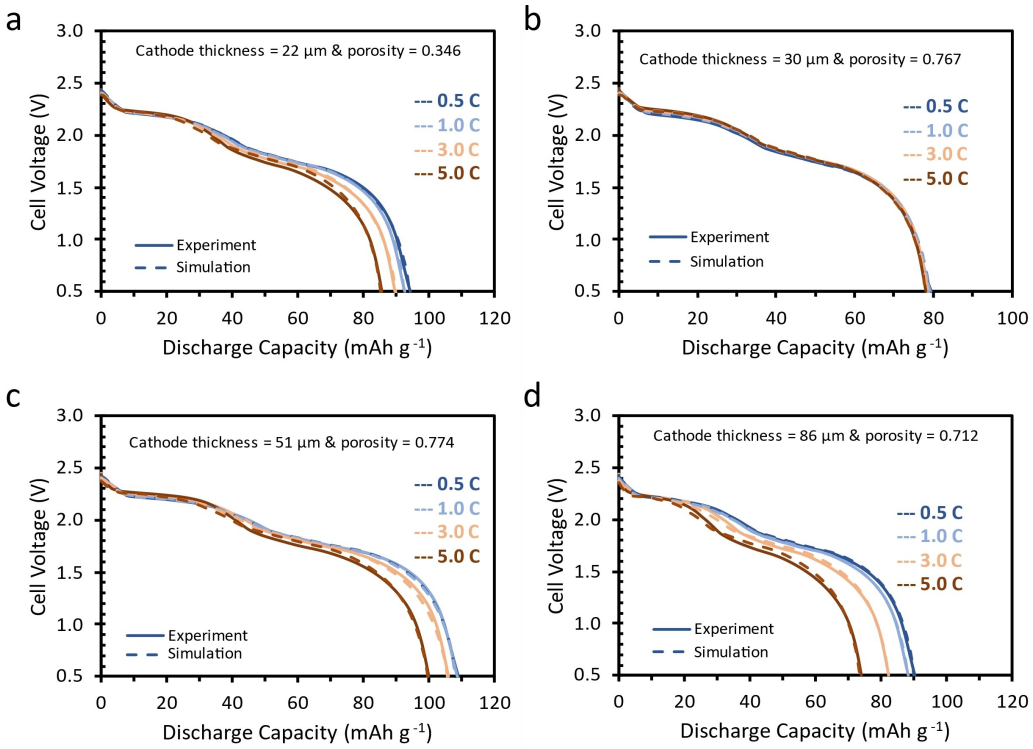

Figure 3. Model validation with experimental data obtained from cells with positive electrode thickness and porosities of a) 22 µm and 0.346, b) 30 µm and 0767, c) 51 µm and 0.774, and d) 86 µm and 0.712, respectively.

high current rates, particularly in cells with thicker and less porous electrodes. This decrease in discharge capacity occurred due to a reduction in species concentration in the positive electrode active material particles, reaching the minimum concentration. This caused a drop in cell voltage to the cutoff potential during discharge.

Parametric analysis

To explore the correlation between the discharge capacity and diffusion of the active species in the various cell designs, we estimated the diffusion coefficients of $AlCl_4^-$ species in the solid phase of the graphite particles, and the effective diffusion coefficient of $AlCl_4^-$ species in the solution phase within the positive electrode by fitting the model predicted discharge profiles to those of the experiments at various discharge current rate and presented the results in Figure 4(a) and (b) respectively. From Figure 4(a), a solid phase diffusion coefficient of

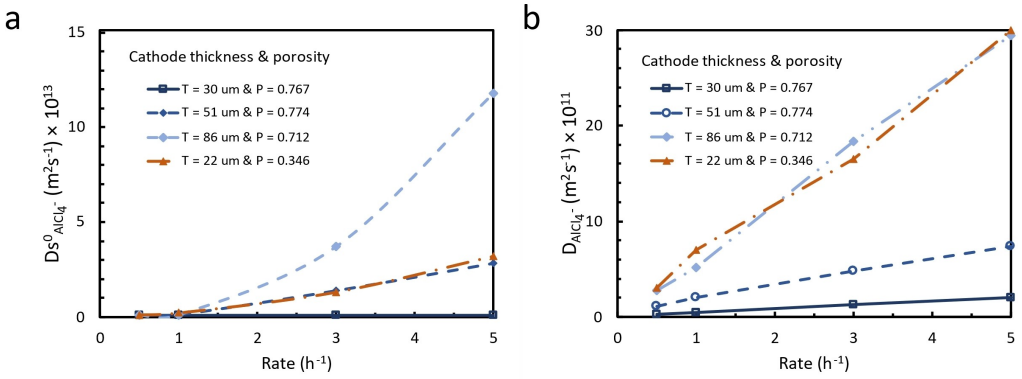

Figure 4. Correlation between transport of electroactive species and various positive electrode designs. Diffusion coefficient of $AlCl_4^-$ species in a) solid phase of the graphite particles and b) solution phase within the positive electrode for Al-graphite cells with different thicknesses and porosities. The values were estimated by fitting the model predictions to the experimental data using the Nelder-Mead least-square fitting algorithm.

Research Article
doi.org/10.1002/batt.202300258
Chemistry Europe
European Chemical Societies Publishing

$D^0_{s\,AlCl_4^-}$, of 1.8×10^{-13} m^2 s^{-1} was suitable for fitting the model prediction to the experimental data at lower current rates (< 3 C). However, for higher current rates (≥3 C), a higher diffusion coefficient was required to fit the model predictions to the experimental data adequately. The effect was pronounced in cells with thicker electrodes. A similar trend was observed in the effective diffusion coefficient of the species in the solution phase within the positive electrode, $D_{AlCl_4^-}$ in Figure 4(b). The results depicted in Figure 4 indicate that the transport of $AlCl_4^-$ species increases in both the solid and solution phases with an increase in the thickness of the positive electrode, and the rate of growth is strongly influenced by the current density. That is, an increase in the positive electrode thickness resulted in an increase in current density (1 C = 120 mA g^{-1}), which led to a faster depletion of the $AlCl_4^-$ species in the cells with a thicker positive electrode than those with a thinner positive electrode, hence the observed relatively poor rate performance in Figure 4.

Figure 5(a) shows the simulated Ragone plots for the Al-graphite cells with different positive electrode thicknesses and porosities. The mass employed here is the total mass of the graphite active material and the mass of the electrolyte. We used the relation given by Kravchyk et al.[2] to estimate the total capacity. We considered an average cell voltage, V_{avg}, of 1.8 V to estimate the specific energy ($C_{total} \times V_{avg}$).

$$C_{total} = \frac{Fx(r-1)C_c}{Fx(r-1) + C_c\left(rM_{AlCl_3} + M_{EMIMCl}\right)} \tag{29}$$

where $F = 26.8{\times}103$ mAh mol^{-1} (Faraday constant), $x = 3/4$ (number of electrons used to reduce 1 mol of the anodic material, i.e., $AlCl_3$), r is the $AlCl_3$:EMIMCl molar ratio, C_C is the specific capacities of the positive electrode in milliampere-hours per gram, M_{AlCl3} is the molar mass of $AlCl_3$ in grams per mole, and M_{EMIMCl} is the molar mass of EMIMCl grams per mole. The specific energies increased with an increase in the positive electrode thickness with an optimum value of ca. 41 Wh kg^{-1} achieved in the cells with a positive electrode thickness of 51 μm and porosity of 0.774. The average specific power did not change significantly with increased positive electrode thickness. However, the observed specific energy will reduce drastically when the mass of the other components of the cell casing are considered. Nevertheless, the location of the knee, which is the plot region corresponding to higher specific energy and average specific power, remained unchanged as the positive electrode thickness increased, suggesting that this type of battery is good for high-power applications.

We simulated the specific energy as a function of positive electrode thickness for different mole ratios, r, of $AlCl_3$:EMIMCl and presented the results in Figure 5(b). The specific energy increased with an increase in r values. Still, the specific energy remained constant at a given r value with increased positive electrode thickness until a critical thickness where diffusion became a limiting factor. At this critical thickness, the diffusion length for the $AlCl_4^-$ species was longer and prevented the complete deintercalation of the $AlCl_4^-$ species from the positive electrode. Consequently, the electrochemical reaction goes into completion before the kinetic reaction, and the cell reaches the minimum cutoff potential earlier than expected. The value of the critical thickness also increases with an increase in the mole ratio, r, because for Al-graphite batteries, the cell's capacity depends on the amount of the ionic species, $AlCl_4^-$, in the electrolyte.

To design an electrode for a specific application, the first step is to identify the ideal electrode thickness and porosity based on the discharge time.[2] To achieve this, we varied the positive electrode's thickness and porosity while holding all other cell design factors constant. Discharge time is a crucial factor in battery design and depends on the battery's intended purpose. Once we determined the discharge time, we selected the positive electrode's thickness and porosity and identified the current at which the cell would reach its 0.5 V cutoff potential at the specified discharge time. The optimal current was determined via a trial-and-error method. After that, we computed the specific energy for that design and repeated the process to calculate the specific energy for a new design. This process was continued until the maximum current density and the reduction in specific energy for a given discharge time had been established.

In Figure 6, the specific energy and current density of various cell designs are plotted against the positive electrode

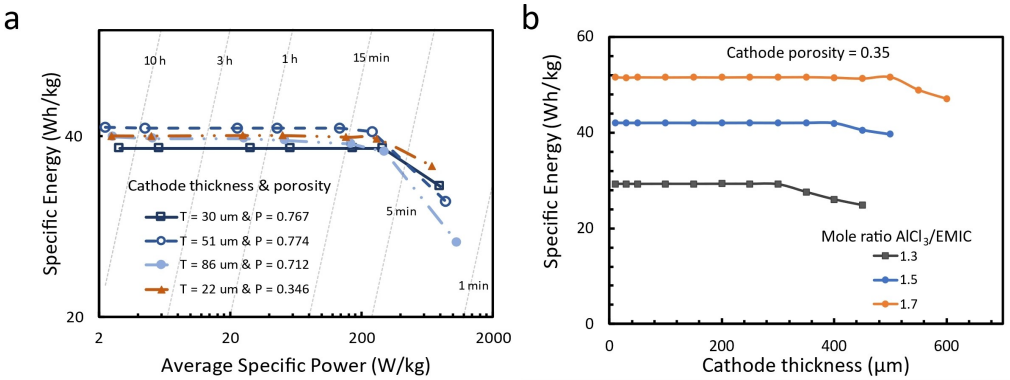

Figure 5. a) Simulated Ragone plot for Al-graphite cell with different positive electrode thickness and porosities and b) Simulated specific energy as a function of positive electrode thickness for different mole ratios of $AlCl_3$/EMIMCl.

Research Article
doi.org/10.1002/batt.202300258
Chemistry Europe
European Chemical Societies Publishing

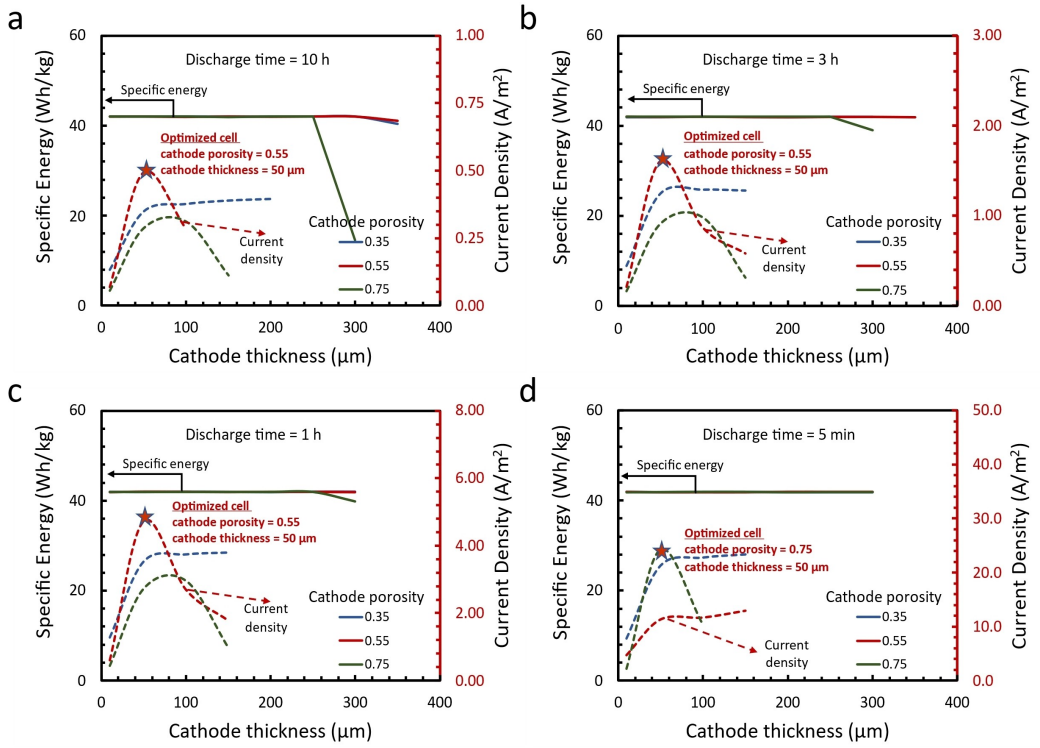

Figure 6. Specific energy and current density of the various cell design as a function of positive electrode thickness for a discharge time of a) 10 h, b) 3 h, c) 1 h and d) 5 min.

thickness for four discharge times. The Al negative electrode thickness and the mole ratio of $AlCl_3$:EMIMCl were held constant while varying the positive electrode thickness and porosity. It was observed that increasing the positive electrode thickness did not significantly impact the specific energy, particularly at lower discharge times and high porosities. However, the current density increased with an increase in positive electrode thickness until an optimal value was reached, after which it began to decline. The optimization process stopped once the optimal value was achieved. No optimal value was found for cells with a porosity of 0.35, but the current density increased to a certain point and remained constant for the remaining positive electrode thicknesses. Nevertheless, in all cases, these current density values were lower than those obtained for the optimal positive electrode porosity. The current density was affected by the positive electrode thickness because the thickness is directly proportional to the positive electrode mass, increasing current density as thickness increases. However, as the positive electrode thickness increased beyond the optimal thickness, the current density decreased, enabling the cell voltage to reach the cutoff voltage at the given discharge time. The optimal thickness obtained for all discharge times considered was 50 µm, similar to the optimal thickness obtained experimentally. The optimal porosity for the cell designed for a 10 h, 3 h, and 1 h discharge time was 0.55, as shown in Figure 6(a), (b), and (c), respectively. The optimal porosity for the cell designed for a 5 min discharge time application was 0.75, as seen in Figure 6(d).

Conclusion

An effective implementation of a specific battery chemistry for a particular application necessitates an appropriate cell design. In this study, we developed a high-fidelity physics-based model to optimize the design of Al-graphite batteries with EMIMCl-$AlCl_3$ IL electrolyte. The model was validated with experimental data obtained from Swgelok cells with different graphite positive electrode thicknesses and porosities. Parametric analysis of the transport parameters suggested that at high current density and in thicker graphite electrodes, the diffusion of the electroactive species was faster, and the cell performance strongly depended on the initial concentration of the electroactive species, $AlCl_4^-$, in the IL electrolyte. Simulation of Ragone plots where the specific energy and average specific power were calculated at the end of the complete discharge showed that the cell performance was suitable for a high-power application based on the knee point. An optimization process was initiated to determine the optimum thickness and porosity for a given application based on the discharge time. The optimization studies showed that the optimum thickness of the graphite positive electrode was 50 µm, and an optimum porosity of 0.55 and 0.75 were obtained for applications requiring slower and faster discharge times, respectively. Determining the optimal electrode design for Al-graphite batteries using different IL electrolytes across various discharge durations would provide valuable guidance in assessing the suitability of a specific IL electrolyte for a particular application.

Research Article
doi.org/10.1002/batt.202300258
Chemistry Europe
European Chemical Societies Publishing

Experimental Section

Materials

Graphite (325 mesh Alfa Aeser, 99.8%), polyvinylidene fluoride (PVDF) 5130 (Solvey), and N-methyl-2-pyrrolidone (NMP) (Sigma) were used to form the electrode ink. Mo Foil (Advent research materials, 99.95%) and Al foil (Alfa Aesar, 99.997%) were used as current collectors. 1-Ethyl-3-methylimidazolium chloride-aluminum chloride (EMIM) (Merck, $\leq$100 ppm iron) was used as the electrolyte.

Electrode preparation

Electrode inks were prepared using graphite and PVDF in a 9:1 ratio. Typically, components were weighed into a 12 mL polytetrafluoroethylene pot and hand mixed for 1 minute. Then, NMP was added in a solid-to-solvent ratio of approximately 1:1.7. The ink was then mixed at 2000 rpm for 5 minutes in an Intertronics Thinky ARE150. This was repeated three times. The resultant ink was then cast onto Mo foil at different blade heights, depending upon the desired loading/thickness. The coating was dried at 80 °C on a hotplate, followed by 2 hrs in a vacuum oven at 80 °C. After, 11 mm discs were cut, placed into individual Al foil packets, and dried in a Büchi tube at 120 °C overnight at $\approx 5\times10^{-3}$ mbar.

Cell preparation and assembly

12 mm discs of glass fiber grade F (GF/F) and 11 mm Al foil discs were cut and dried in a Büchi tube at 120 °C for 1–3 days and, subsequently, transferred into an Ar glovebox (M.Braun, Unilab) (O2 and H2O $<$ 0.1 ppm). Swagelok cell casings, consisting of a tungsten bar (working electrode side), aluminum bar and cap (reference/counter side), and an aluminum cell body (lined with Mylar), were sanded with ethanol using 1200 grit sandpaper followed by sonication (RS PRO 3 L, 100 W) for 20 minutes. These were dried overnight at 70 °C at 1 atm. The tungsten side of the Swagelok cell was then assembled, and all cell components were placed in a vacuum oven at 80 °C for two hours before being transferred into the glovebox.

Once all components were transferred, electrodes were weighed (Kern - ABT 120 5DNM) to four decimal places. Therefore, the balance error was $\pm$0.05 mg. The electrodes were placed upon the pre-constructed tungsten side of the Swagelok cell. Two GF/F discs were added followed by 120 μL of the electrolyte. The Al counter/reference electrode was placed on top. The aluminum cap was added, and an Al spring inserted followed by the Al rod. The cell was then sealed by hand tightening.

Electrochemical characterization

All cells were cycled at 25 °C in either a Memert HPP-110 or a Binder MK series climatic chamber using a biologic VMP3 or VMP2 potentiostat. Cells were assessed by galvanostatic cycling with potential limitation (GCPL) after a 15hr rest at open circuit voltage. A specific current (normalized to the mass of graphite) was applied using the following regime: 60 mA g^{-1} (21 cycles), 120 mA g^{-1} (21 cycles), 60 mA g^{-1} (11 cycles), 360 mA g^{-1} (21 cycles), 60 mA g^{-1} (11 cycles) and 600 mA g^{-1} (21 cycles). An upper and lower potential range between 2.45 and 0.5 V, respectively, was applied.

Acknowledgements

The authors acknowledge the financial support for this work from the European Commission through the Horizon 2020 FET-Proactive project AMAPOLA (grant agreement No. 951902). We also thank Prof. Nuria Garcia-Araez for her constructive comments and discussions on this work.

Conflict of Interests

The authors declare no conflict of interest.

Data Availability Statement

The data that support the findings of this study are available from the corresponding author upon reasonable request.

Keywords: aluminum graphite batteries · ionic liquid electrolytes · optimization · physics-based model · Ragone plot

[1] M. C. Lin, M. Gong, B. Lu, Y. Wu, D. Y. Wang, M. Guan, M. Angell, C. Chen, J. Yang, B. J. Hwang, H. Dai, *Nature* **2015**, *520*, 325.
[2] K. V. Kravchyk, S. Wang, L. Piveteau, M. V. Kovalenko, *Chem. Mater.* **2017**, *29*, 4484.
[3] S. Wang, K. V. Kravchyk, F. Krumeich, M. V. Kovalenko, *ACS Appl. Mater. Interfaces* **2017**, *9*, 28478.
[4] X. Zhang, S. Wang, J. Tu, G. Zhang, S. Li, D. Tian, S. Jiao, *ChemSusChem* **2018**, *11*, 709.
[5] K. V. Kravchyk, C. Seno, M. V. Kovalenko, *ACS Energy Lett.* **2020**, . $<$5$>$ $<$ 545$>$ Dear Author, if the journal has volumes, please add the journal number. $<$5$>$ $<$545$>$
[6] Y. Song, S. Jiao, J. Tu, J. Wang, Y. Liu, H. Jiao, X. Mao, Z. Guo, D. J. Fray, *J. Mater. Chem. A* **2017**, *5*, 1282.
[7] F. Ambroz, T. J. Macdonald, T. Nann, F. Ambroz, T. J. Macdonald, T. Nann, *Adv. Energy Mater.* **2017**, *7*, 1602093.
[8] F. Wu, H. Yang, Y. Bai, C. Wu, F. Wu, H. Yang, Y. Bai, C. Wu, *Adv. Mater.* **2019**, *31*, 1806510.
[9] Z. A. Zafar, S. Imtiaz, R. Razaq, S. Ji, T. Huang, Z. Zhang, Y. Huang, J. A. Anderson, *J. Mater. Chem. A* **2017**, *5*, 5646.
[10] W. Zhou, M. Zhang, X. Kong, W. Huang, Q. Zhang, *Adv. Sci.* **2021**, *8*, 2004490.
[11] O. M. Leung, T. Schoetz, T. Prodromakis, C. P. de Leon, *J. Electrochem. Soc.* **2021**, *168*, 056509.
[12] E. Faegh, B. Ng, D. Hayman, W. E. Mustain, *Nat. Energy* **2021**, *6*, 21.
[13] W. A. Appiah, J. Park, S. Song, S. Byun, M. H. Ryou, Y. M. Lee, *J. Power Sources* **2016**, *319*, 147.
[14] V. Srinivasan, J. Newman, *J. Electrochem. Soc.* **2004**, *151*, A1530.
[15] J. Tu, W. L. Song, H. Lei, Z. Yu, L. L. Chen, M. Wang, S. Jiao, *Chem. Rev.* **2021**, *121*, 4903.
[16] D. Diddens, W. A. Appiah, Y. Mabrouk, A. Heuer, T. Vegge, A. Bhowmik, D. Diddens, Y. Mabrouk, A. Heuer, W. A. Appiah, T. Vegge, A. Bhowmik, *Adv. Mater. Interfaces* **2022**, *9*, 2101734.
[17] W. Mei, H. Chen, J. Sun, Q. Wang, *Sustain. Energy Fuels* **2018**, *3*, 148.
[18] W. A. Appiah, Y. Roh, C. B. Dzakpasu, M.-H. Ryou, Y. M. Lee, *J. Electrochem. Soc.* **2020**, *167*, 080542.
[19] M. Duquesnoy, C. Liu, D. Z. Dominguez, V. Kumar, E. Ayerbe, A. A. Franco, *Energy Storage Mater.* **2023**, *56*, 50.
[20] R. P. Cunha, T. Lombardo, E. N. Primo, A. A. Franco, *Batteries & Supercaps* **2020**, *3*, 60.
[21] J. Jeong, H. Lee, J. Choi, M. H. Ryou, Y. Min Lee, *Electrochim. Acta* **2015**, *154*, 149.
[22] C. Heubner, A. Nickol, J. Seeba, S. Reuber, N. Junker, M. Wolter, M. Schneider, A. Michaelis, *J. Power Sources* **2019**, *419*, 119.
[23] J. Newman, W. Tiedemann, *AIChE J.* **1975**, *21*, 25.

[24] W. A. Appiah, A. Stark, S. Lysgaard, J. Busk, P. Jankowski, J. H. Chang, A. Bhowmik, B. Gollas, J. M. Garcia-Lastra, *Chem. Eng. J.* **2023**, *472*, 144995.
[25] T. Jiang, M. J. Chollier Brym, G. Dubé, A. Lasia, G. M. Brisard, *Surf. Coat. Technol.* **2006**, *201*, 1.
[26] C. Ferrara, V. Dall'asta, V. Berbenni, E. Quartarone, P. Mustarelli, **2017**, DOI 10.1021/acs.jpcc.7b07562. <121> <26607> Dear author, please check this journal. <121> <26607>
[27] G. A. Elia, N. A. Kyeremateng, K. Marquardt, R. Hahn, *Batteries & Supercaps* **2019**, *2*, 83–90.
[28] J. Lampkin, H. Li, L. Furness, R. Raccichini, N. Garcia-Araez, *ChemSusChem* **2020**, *13*, 3514.
[29] R. Böttcher, A. Ispas, A. Bund, *Electrochim. Acta* **2021**, *366*, 137370.
[30] W. A. Appiah, H. Li, J. Lampkin, J. M. García-Lastra, *J. Power Sources* **2022**, *529*, 231254.
[31] W. A. Appiah, J. Busk, T. Vegge, A. Bhowmik, *Electrochim. Acta* **2023**, *439*, 141430.

Manuscript received: June 20, 2023
Revised manuscript received: September 22, 2023
Accepted manuscript online: September 26, 2023
Version of record online: October 18, 2023